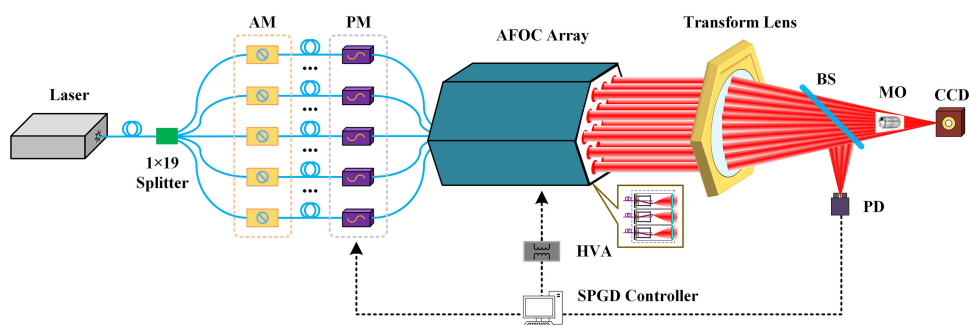


Experimental Demonstration of Central-Lobe Energy Enhancement Based on Amplitude Modulation of Beamlets in 19 Elements Fiber Laser Phased Array







Volume 13, Number 3, June 2021

Jing Zuo
Feng Li
Chao Geng
Fan Zou
Jiali Jiang
Jiaying Liu
Xu Yang
Tao Yu
Guan Huang
Zhihua Fan
Bincheng Li
Xinyang Li



DOI: 10.1109/JPHOT.2021.3071230

Experimental Demonstration of Central-Lobe Energy Enhancement Based on Amplitude Modulation of Beamlets in 19 Elements Fiber Laser Phased Array

Jing Zuo ^{1,2,3}, Feng Li ^{1,2}, Chao Geng ^{1,2}, Fan Zou ^{1,2,3},
Jiali Jiang^{1,2}, Jiaying Liu^{1,2,3}, Xu Yang^{1,2,3}, Tao Yu^{1,2,3},
Guan Huang ^{1,2,3}, Zhihua Fan⁵, Bincheng Li ⁴ and Xinyang Li^{1,2}

¹Key Laboratory on Adaptive Optics, Chinese Academy of Sciences, Chengdu 610209, China

²Institute of Optics and Electronics, Chinese Academy of Sciences, Chengdu 610209, China

³University of Chinese Academy of Sciences, Beijing 100049, China

⁴University of Electronic Science and Technology of China, Chengdu 611731, China

⁵Sichuan University of Arts and Science, Dazhou 635000, China

DOI:10.1109/JPHOT.2021.3071230

This work is licensed under a Creative Commons Attribution 4.0 License. For more information, see <https://creativecommons.org/licenses/by/4.0/>

Manuscript received January 8, 2021; revised March 29, 2021; accepted April 1, 2021. Date of publication April 6, 2021; date of current version April 22, 2021. This work was supported by the National Natural Science Foundation of China under Grants 61675205 and 62005286. Corresponding author: Chao Geng (e-mail: blast_4006@126.com).

Abstract: Coherent beam combination of fiber laser phased array is a promising technique to achieve high-brightness laser output. In this paper, we focus on central-lobe energy enhancement of the combined beam in the far-field by theoretically and experimentally investigating the relationship between the power-in-the-bucket (PIB) of the combined beam in the far-field and the beamlets amplitude modulation in the near-field. We employ a 19-elements fiber laser phased array integrating adaptive fiber-optic collimators with a beamlet filling factor of 0.903 and achieve phase-locking and beamlet pointing correction among fiber lasers using the SPGD algorithm. The amplitude modulation applied to the tiled sub-apertures is used to control the shape of the emissive array's amplitude envelope to further change the PIB of the combined beam under the same total output power. According to theoretical analysis, the fiber laser phased array achieves $PIB = 0.51$ for a zero truncation ratio (Tr), which is increased to $PIB = 0.57$ for $Tr = 1.3$. Experimentally, we observe $PIB = 0.49$ for $Tr = 0$ and $PIB = 0.56$ for $Tr = 1.3$. The experimental results are in good agreement with the theoretical analysis, suggesting that the amplitude modulation is helpful for further improving the energy density of central-lobe.

Index Terms: Coherent beam combination, fiber laser phased array, central-lobe energy enhancement, amplitude modulation.

1. Introduction

Coherent beam combination (CBC) of fiber laser phased array (FLPA) provides an approach for achieving laser output with high energy density and high beam quality [1]–[5]. A nearly diffraction-limited equivalent large-aperture output laser can be obtained by correcting the phase and tip/tilt errors in each sub-aperture of the FLPA. At present, both large-scale FLPA and high-power fiber

laser coherent combining technologies have achieved breakthroughs. Currently, the maximum scaling and maximum combined power of the FLPA are over 100 elements and over 16kW [2], [3]. Although the tip/tilt error control has not been included in these reports, the FLPA with only phase-locking control has shown great potential in improving the brightness of the combined beam. Due to these advantages, several related research projects have been launched in recent years [6]–[9]. For example, in 2006, Mourou *et al.* proposed the International Coherent Amplification Network (ICAN) project in the European Union, aiming to achieve a femtosecond laser with high repetition rate, high average power, and high peak power through coherent combining technology of FLPA [4]. This plan looks forward to the application prospects of the ICAN system in particle acceleration and space debris cleaning.

In FLPA applications, the input electrical power provided to the laser system is sometimes limited. For example, in 2014, Souldard *et al.* proposed to carry the ICAN system in a space vehicle, and the solar panels on the carrying platform provide electrical energy to ICAN to remove space debris [7]. Therefore, it is vital to obtain a higher energy density central lobe in the far-field when the total electrical input power is equal. In fact, the structure of the FLPA is similar to an optical phased array, where amplitude modulation is often used to improve the energy in central lobes [10]–[12]. Recently, Wang *et al.* found that the central-lobe energy of a FLPA system can be enhanced by amplitude modulation in the near-field, to make the amplitude envelope of the beamlets following a nonuniform distribution [13]. However, their work is purely based on numerical calculations, without a mathematical model and experimental demonstration.

In this paper, we propose a central-lobe energy enhancement method via tuning the amplitude envelope of the beamlets in the near-field to further increase the central-lobe energy in the combined beam after the phase and tip/tilt errors are both corrected. Both theoretical model and experimental results of a 19 elements FLPA system are presented to demonstrate the feasibility of the proposed method.

2. Theory and Mathematical Models

2.1 Basic Theory

The amplitude modulation is employed to adjust the characteristics of the central-lobe in far-field in phased array technique and the amplitude coefficients of array wavelets can be obtained indirectly by solving the radiation field of the equivalent single large-aperture electromagnetic wave [14], [15]. According to the feature that the array is formed by splicing multiple wavelets, the amplitude coefficients of the array wavelets can be obtained by sampling the amplitude of the equivalent single large-aperture wave-front. Until now, the effects of uniform and non-uniform amplitude distribution (Chebyshev distribution, Taylor distribution, and Gaussian distribution) on the central-lobe enhancement has been compared in microwave phased array techniques. The results confirm that a non-uniform distribution ratio in the emissive beam provides better performance than the uniform distribution and the Gaussian distribution allows one to achieve a better suppression effect than the other two distributions. Similar to microwaves, light waves also belong to the electromagnetic wave, and the physical characteristics of the two are usually consistent [16]. Therefore, we can directly analyze the radiation characteristics of the beamlet array in the far-field by analyzing the radiation characteristics of the Gaussian beam with the same diameter as the circumscribed circle of the beamlet array in the far-field, and then use stochastic parallel gradient descent (SPGD) algorithm to directly optimize the amplitudes of the outgoing beamlets in CBC system so that the effect of beamlet amplitude modulation can be verified [17], [18].

Fig. 1 shows a schematic diagram of the plane of a hexagonal array. The parameters describing the emissive array of 19 elements FLPA are as follows: the 19 sub-apertures are arranged in a regular hexagonal array in a circle of radius $R = 76$ mm. The sub-aperture diameter $d = 28$ mm, and the distance between the centers of adjacent sub-apertures $s = 31$ mm. The operating wavelength $\lambda = 1064$ nm.

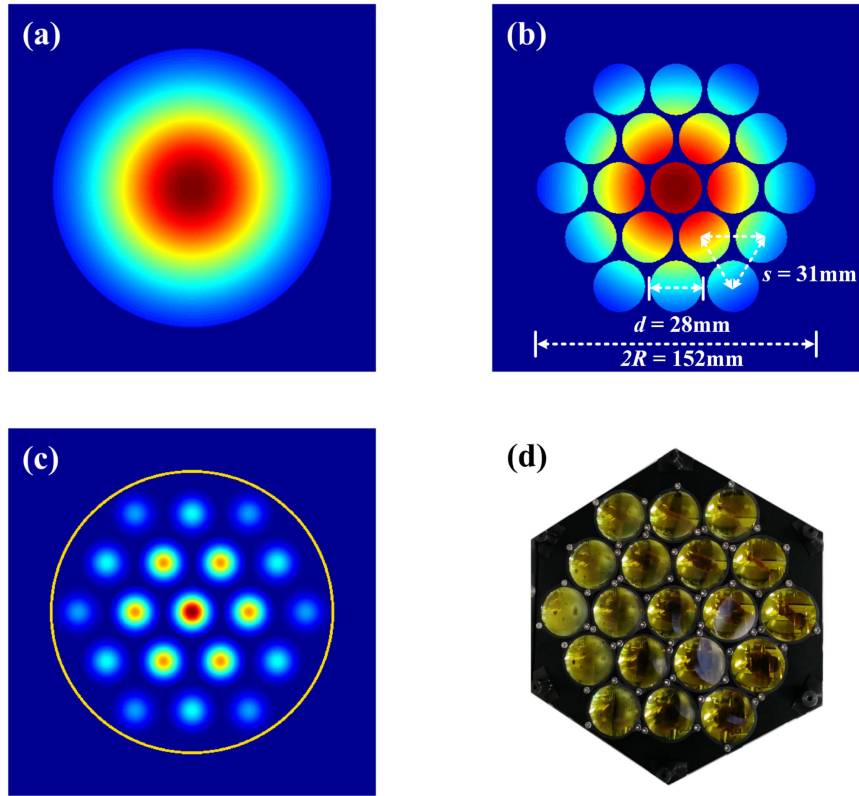


Fig. 1. Schematic diagram and real picture of the emissive hexagon array plane of a 19 elements FLPA system. (a) Equivalent Gaussian beam, (b) Sampled equivalent Gaussian beam, (c) Emissive plane of 19-element FLPA, and (d) Real picture of the emissive hexagonal array plane.

2.2 Diffraction Model of Single Gaussian Beam

The complex amplitude distribution of a Gaussian beam in the Fraunhofer diffraction region is analyzed [19]–[21]. According to the Fresnel-Kirchhoff diffraction principle, the distribution of the light field at any point $P(x, y')$ in the far-field is given by

$$E_{far}(P) = \iint E_{near}(x, y) \exp\left[\frac{-ik(xx' + yy')}{z}\right] dx dy \quad (1)$$

Where $E_{near}(x, y)$ is the complex amplitude, $Q(x, y, 0)$ and $P(x, y', z)$ stand for the points of the near-field coordinate plane and of the far-field coordinate plane, respectively.

$$E_{near}(x, y) = A \exp\left[-\frac{x^2 + y^2}{\Omega^2(z)}\right] \exp\left[-i\frac{k}{2r}(x^2 + y^2)\right] \quad (2)$$

$$\Omega(z) = \Omega_0 \left[1 + \frac{z^2}{z_0^2}\right], \quad r = z_0 \left[1 + \frac{z^2}{z_0^2}\right], \quad k = \frac{2\pi}{\lambda}, \quad z_r = \frac{\pi\Omega_0^2}{\lambda}$$

To simplify the analysis, we assume the Gaussian beam's waist Ω_0 is in the pupil plane and the pupil position is at z_0 is the distance from the Gaussian beam waist to the diffraction screen. A is the amplitude coefficient, k is the wave number, and z_r is the Rayleigh distance.

Moving to polar coordinates $Q(\rho, \varphi, 0)$ and $P(\rho', \varphi', z)$ we may rewrite Eq. (1) as follows

$$\begin{aligned} E_{far}(P) &= \int_0^{2\pi R} \int_0^2 A \exp\left(-\frac{\rho^2}{\Omega_0^2}\right) \exp\left(\frac{-ik\rho\rho' \cos(\varphi - \varphi')}{z}\right) \rho d\rho d\varphi \\ &= \pi R^2 A \exp(-R^2/\mu^2) \left\{ \frac{2J_1(vR)}{(vR)} + \frac{2^2 J_2(vR)R^2}{(vR)^2 \mu^2} + \dots \right\} \\ &= 2\pi A \int_0^R \exp\left(-\frac{\rho^2}{\Omega(z)^2}\right) \exp\left(-ik\frac{\rho^2}{2r}\right) J_0\left(\frac{k}{z}\rho\rho'\right) \rho d\rho \end{aligned} \quad (3)$$

Where the pupil aperture is a circular hole with radius $R = 76\text{mm}$, J_0 is a zero-order Bessel function and $\mu^2 = \Omega^{-2} + \frac{ik}{2r}$, $v = \frac{k\rho'}{z} \approx k \sin \theta$.

According to the definition of beam intensity ($I_{far}(P) = E^*(P) \cdot E(P)$), the beam intensity at point P in the far-field is given by

$$\begin{aligned} I_{far}(P) &= I_0 \left\{ \left[\sum_{n=1}^{\infty} \frac{2^n J_n(kR \sin \theta)}{(kR \sin \theta)^n} \left(\frac{R^2}{\Omega \Omega_0}\right)^{n-1} \cdot \cos(n-1)\psi \right]^2 \right. \\ &\quad \left. + \left[\sum_{n=1}^{\infty} \frac{2^n J_n(kR \sin \theta)}{(kR \sin \theta)^n} \left(\frac{R^2}{\Omega \Omega_0}\right)^{n-1} \cdot \sin(n-1)\psi \right]^2 \right\} \end{aligned} \quad (4)$$

Where, $I_0 = \pi A^2 R^2 \exp(-\frac{R}{\Omega_0^2})^2$, $\psi = \arctan(z_0/z_r) = \arctan[(\Omega^2 - \Omega_0^2)^{1/2}/\Omega_0]$

Upon inspecting Eq. (4), one may see that the beam intensity distribution in the Fraunhofer diffraction region is regulated by the pupil's size (R) and the Gaussian beam waist Ω_0 . The truncation ratio ($Tr = R/\Omega_0$) is used to describe the relationship between R and Ω_0 . n is the order of the Bessel function J_n and when $Tr = 0$, higher-order terms with $n = 2$ and above can be ignored.

$$I_{far}(P) = I_0 \left[\frac{2J_1(kR \sin \theta)}{kR \sin \theta} \right]^2 \quad (5)$$

Equation (5) is the formula of far-field beam intensity distribution of flat-top beam. By looking at Eqs. (4) and (5), one may appreciate the difference between a Gaussian beam and a flat-top beam in the far-field: the Gaussian beam's diffraction field is formed by superimposing Bessel functions of various orders, which have no common zeros. Because of this, the peak power of the first-order diffraction ring decreases and its zero-point position expands outward. The energy in the first-order diffraction ring thus increases and the ring size increases. At the same time, the energy of the secondary diffraction ring is reduced.

An index to evaluate the quality of laser transmission is the average power density in the far-field, which is generally characterized by power-in-the-bucket (PIB). It is defined as the ratio of the combined beam's power in the bucket to the total power of the combined beam. The bucket size d_{bucket} ($d_{bucket} = 1.22\lambda/R$) is the diffraction-limited diameter.

$$PIB = \frac{\iint_{\text{circ}(d_{bucket})} I_{far}(x', y') dx' dy'}{\iint I_{far}(x', y') dx' dy'} \quad (6)$$

Fig. 2(a) shows the behavior of PIB for different Tr values. When $Tr = 0$, it means that Ω_0 is infinity, and the amplitude shape of the single beam is flat-top type, which is widely used in high power laser system. In this state, we have $PIB = 0.8378$. The maximum PIB 0.9691 occurs at $Tr = 1.3$, which is 0.1313 higher than that at $Tr = 0$. In Fig. 2(b), when $Tr = 1.3$, it can be seen that the far-field spot becomes wider and the peak energy decreases compared to the case of $Tr = 0$. This effect is more obvious as Tr further increases. When $Tr = 2.5$, diffraction is very weak, which indicates that the circular hole has almost no limit to the incident beam and that the intensity distribution curve is the result of the direct projection of the incident Gaussian beam.

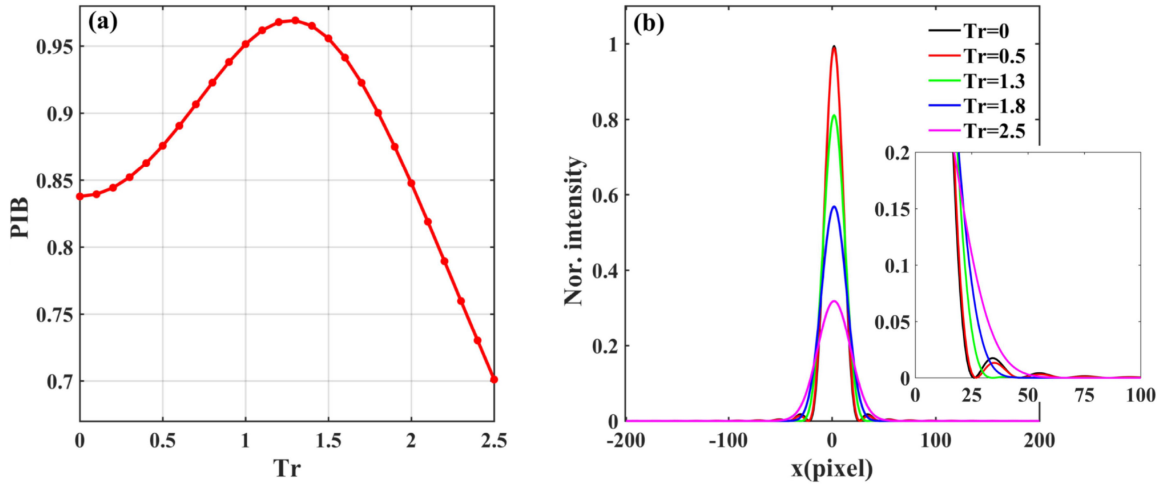


Fig. 2. Beam quality of a single Gaussian beam in far-field with different Tr (a) PIB versus Tr and (b) One-dimensional intensity distribution of the single beam.

2.3 Mathematical Model of FLPA System

The CBC of the FLPA system can be viewed as a multi-beam interference [22]–[24]. To specifically study the effect of central-lobe energy enhancement based on amplitude modulation of beamlets, we assume that there are no phase errors and tip/tilt errors in the system, and the beamlets are derived from the same seed laser source. As it is shown in Fig. 1, the amplitude of each beamlet can be adjusted to match the intensity of a specific envelope at different Tr. The near-field complex amplitude of the n th beamlet U_n can be expressed as

$$U_n(x, y, z) = A_n \frac{\omega_0}{\omega(z - z_n)} \exp \left[-\frac{(x - x_n)^2 + (y - y_n)^2}{\omega^2(z - z_n)} \right] \quad (7)$$

The far-field intensity distribution of the coherent combined beam is

$$I(x', y', z) = U(x', y', z) \cdot U^*(x', y', z) \quad (8)$$

Where

$$U(x', y', z) = \sum_1^n U_n(x', y', z) \quad (9)$$

and (x_n, y_n, z_n) are the coordinates of the n th beam at the emissive surface. z is the distance traveled by the laser beam and the z -plane is the coherent focal plane. $\omega_0 = 11$ mm, which is the waist radius of beamlet in the emissive plane. A_n is the amplitude of the n th sub-aperture beam, which can be used to adjust the intensity to a specific distribution (Tr). The centers of the whole sub-apertures are arranged in circles of four different diameters from the center sub-aperture to the outside, such that there are only four levels of amplitude index A_n that need to be adjusted, as shown in Fig. 3.

Fig. 4 shows the PIB of the 19 elements FLPA and the variation of the central-lobe widths of the combined spots. When $Tr = 0$, the amplitudes of the outgoing beamlets are equal and we have $PIB = 0.51$. Different Tr represents different amplitude envelope shape of outgoing beamlets and by changing the value of A_n , the amplitude of each beamlet can be adjusted to a specific distribution. Keeping the total output power constant, and when $Tr = 1.3$ we have $PIB = 0.57$, which is the maximum value. The difference between the two cases is that PIB of the FLPA system in Fig. 4(a) is generally smaller than the PIB value of the equivalent beam, which is caused by the cut effect and the arrangement of sub-apertures of the array. To improve the combining efficiency,

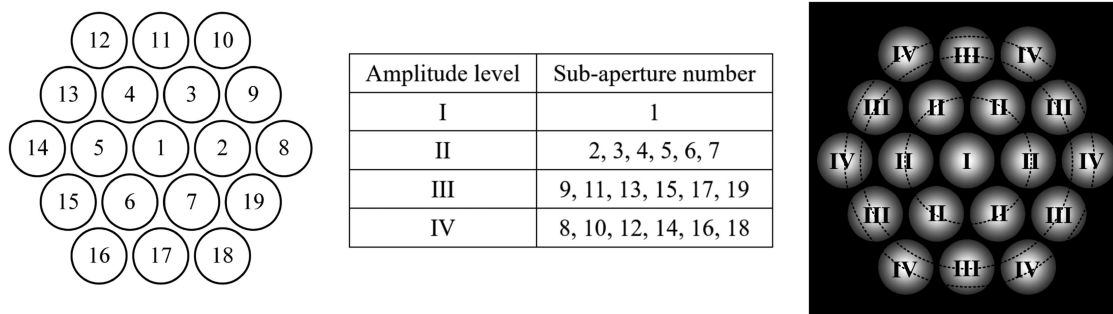


Fig. 3. Four amplitude levels of 19-element FLPA system.

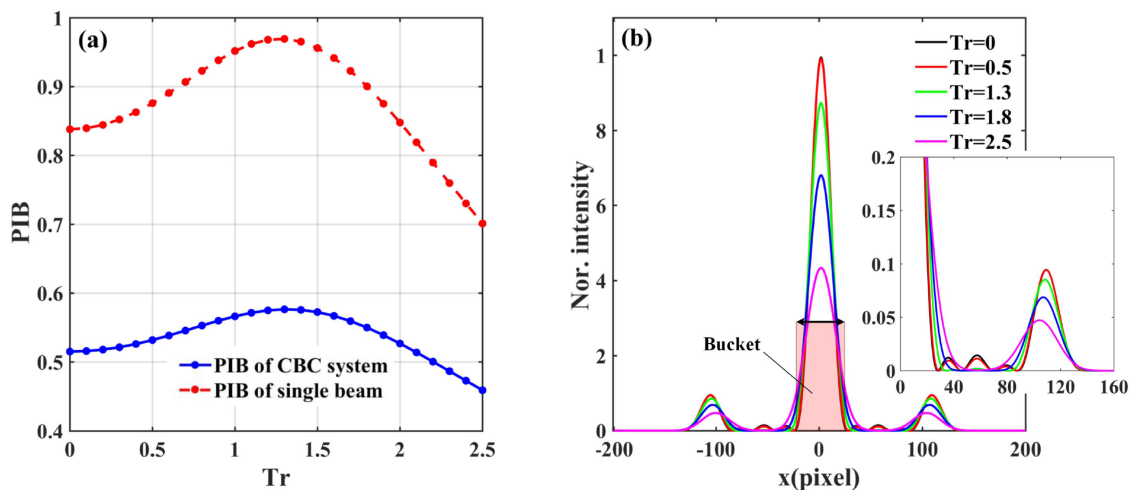


Fig. 4. Far-field cost function of 19 Gaussian beamlets with different Tr (a) PIB versus Tr and (b) One-dimensional intensity distribution of the combined beams.

the Gaussian beamlet ω_0 is cut to obtain a more uniform intensity distribution wave-front in each sub-aperture. However, the energy of outgoing beamlets will be decreased by cut operation. The energy transmission efficiency η (defined as the ratio of transmission power to the total power) reflects the power loss of the fiber array and is related to the diameter of the sub-aperture d in which $\eta(d) = 1 - \exp[-(d/2\omega_0)^2]$. It is contradictory to increase the PIB and η at the same time and when the sub-aperture diameter d is 28 mm, the system has a higher PIB value and lower power loss. Moreover, there are some gaps between the sub-apertures, this also causes PIB of the array beamlets to be lower than PIB of the equivalent single beam. However, the changing trend of the spot width in the far-field is consistent.

In order to check whether the Gaussian distribution is the best, we directly optimize the beamlet amplitude of the CBC system using SPGD algorithm [25]. It can be seen that the optimized result is very close to PIB value at $Tr = 1.3$, as shown in Fig. 5. The energy of the central-lobes of the combined spots is indeed increased under the same total emissive power.

2.4 Phenomenon in Different Scale Arrays

For the regular hexagonal FLPA system with a filling factor of 0.903 (defined as the ratio of sub aperture diameter to center distance of adjacent aperture), the relationship between the scale of the array and PIB is analyzed. By applying the same method mentioned above, PIB values

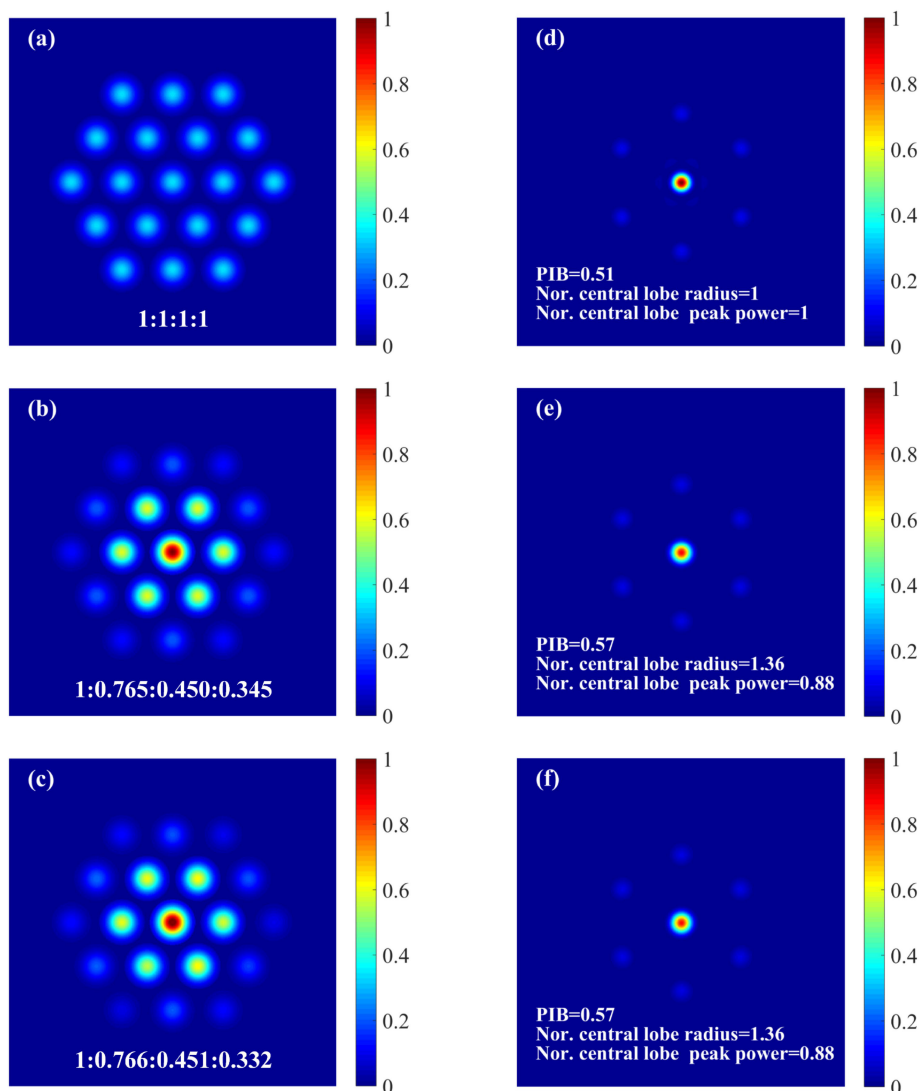


Fig. 5. Near-field (left) and far-field (right) pattern of 19-element FLPA system with different Tr . (a)(d) $Tr = 0$, (b)(e) $Tr = 1.3$ and (c)(f) SPGD optimized results.

corresponding to CBC systems with 7, 19, 37, and 61 fiber lasers are obtained. The behavior of PIB, together with the combined spot radius and the peak intensity of the emissive array are shown in Fig. 6. The near-field intensity distribution and amplitude ratio of the array are shown in Fig. 7. It can be seen that independent of the array's scale, PIB always is maximum when $Tr = 1.3$, as shown in Fig. 6(a). Figs. 6(b) and 6(c) show the central lobe radius and normalized peak intensity at different array scales. It can be seen that when $Tr = 1.3$, the peak power of the central-lobe in the fiber arrays of different sizes decreases slightly, and the width becomes wider (to be analyzed in Section III).

3. Experimental Results and Discussion

The experimental setup of 19-element FLPA system is illustrated in Fig. 8. The key components for phase lock control and tip/tilt control are homemade [26]. The piezoelectric ceramic ring fiber optic

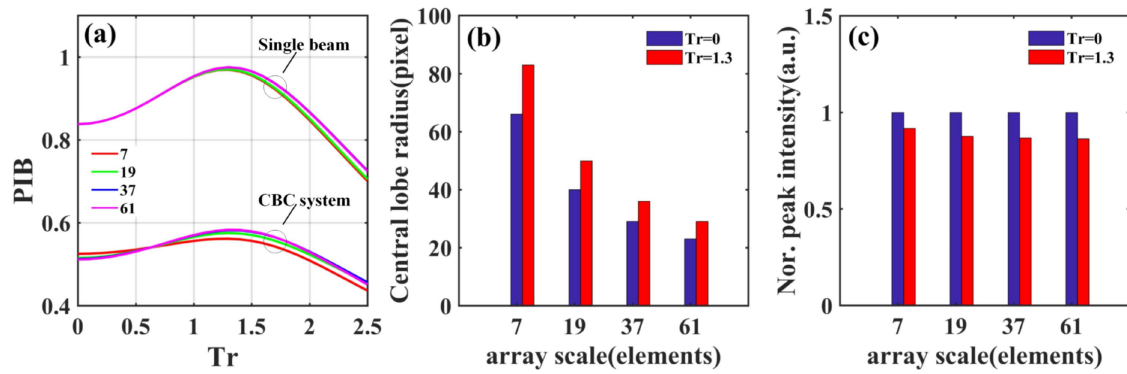


Fig. 6. The performance index of different array scale. (a) PIB, (b) Central lobe radius and (c) Normalized peak intensity.

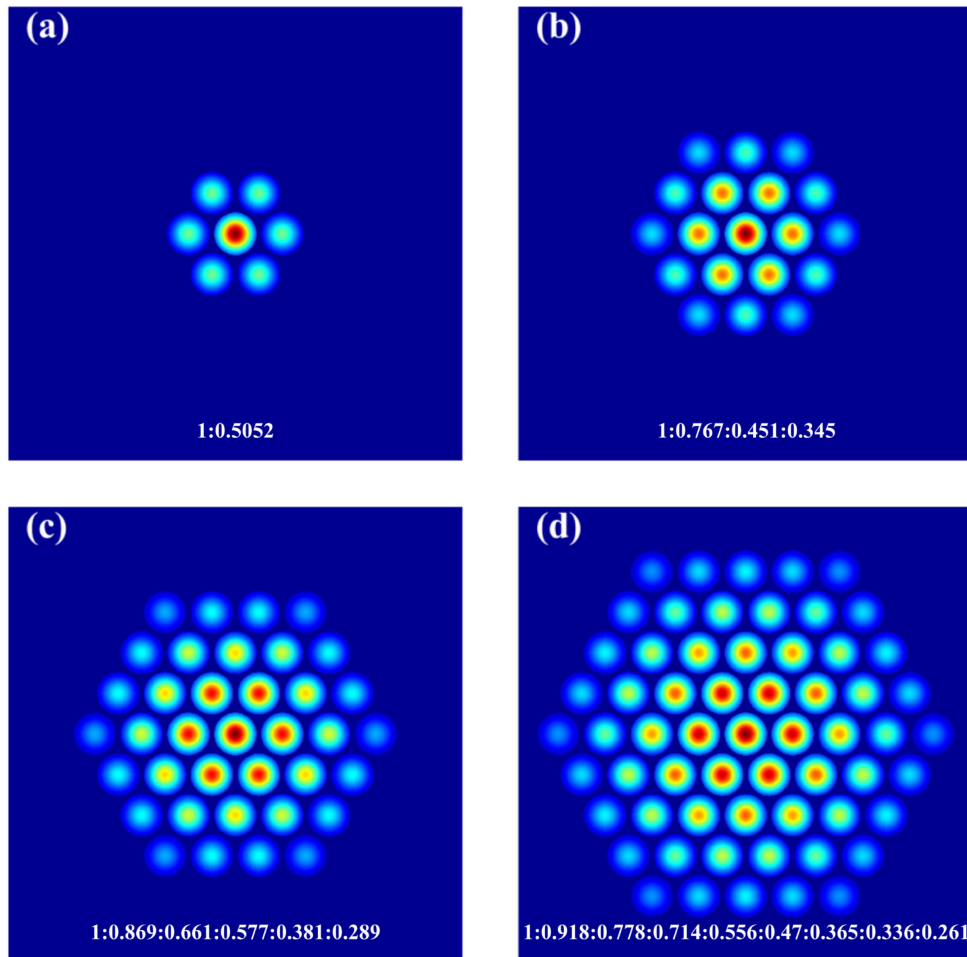


Fig. 7. When $Tr = 1.3$, the amplitude distribution of different scale arrays in the near-field. (a) 7 elements, (b) 19 elements, (c) 37 elements, and (d) 61 elements.

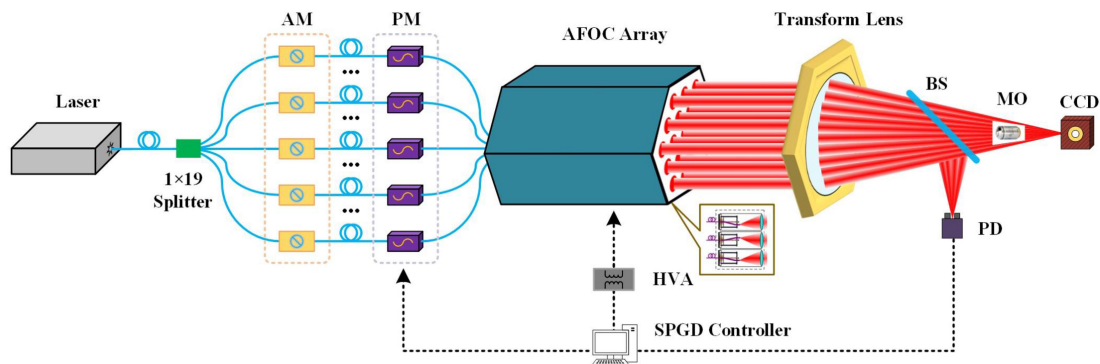


Fig. 8. Schematic diagram of the 19 elements FLPA system.

phase modulator (PM) has a half-wave voltage of approximately 2.5 V and first-order resonance frequency of approximately 32 kHz. The maximum optical-length displacement of the PM is about 4λ with a control voltage from -10 V to 10 V, and the maximum optical power handling is about W-level, with a PM-980 fiber. It is produced by twisting the polarization-maintaining fiber around a piezoelectric ceramic ring. The adaptive fiber optics collimator (AFOC) has an offset range of optical fiber end face $\pm 30\ \mu\text{m}$ and first-order resonance frequency about 2 kHz. The control signal is amplified 100 times by a high-voltage amplifier (HVA) to move the position of the fiber end face at the focal plane of the lens to change the direction of the outgoing beam. The source laser is a linearly polarized single-mode fiber laser at 1064 nm wavelength with a maximum output power of 110 mW and line-width of 20 kHz. The source is equally divided into 19 channels by a fiber splitter, and each one is connected to a PM, which is later employed to correct the phase-type errors of the array. We have also 19 beam amplitude modulators (AM), each one connected to the output of a PM to adjust the final emitted beam intensity of each beamlets. Each AM is connected to the AFOC's tail fiber and then emitted into free space. The 19 beamlets have identical polarization direction, a feature obtained by rotating the fiber tip of each AFOC during assembling. One part is focused by a transform lens with a focal length of 2 m and then the focused beamlets are sent to a beam splitter (BS). After passing through the BS, a part of the beamlet is sent to a $10\times$ micro-objective (MO) and detected by a high-speed CCD camera to observe and calculate the actual PIB. Another part is sent to a photo detector (PD) with a pin hole of $10\ \mu\text{m}$ diameter on the focal plane of the transform lens, used to assess performance index and to produce the cost function for the SPGD controller, which can optimize the phase error and tip/tilt error. Moreover, because the PD has a high sampling rate, the cost function (voltage acquired by PD) can also accurately reflect the control bandwidth (iteration rate), the enhancement capacity of PIB (average value), and the stability of the convergence stage (MSE) during the experiment.

The behavior of a 15 s normalized cost function collected by the PD of the 19-element FLPA is shown in Fig. 9. When the phase error and tip/tilt errors are not corrected, the system is in an open loop state: the average (Ave) of the cost function is 0.0182 and the mean square error (MSE) is 0.0162, where Ave and MSE are dimensionless results. After 36 ms, the system enters the phase-locked state in which the iteration rate is 9.8 kHz (the convergence time of the SPGD algorithm is defined as the time taken for the normalized cost function to reach 90% of the steady state value). When the phase error is corrected and the system is in a closed loop state (PL), the Ave of cost function rises to 0.335 and the MSE decreases from 0.0162 to 0.0021. After 670 ms, the phase errors and tip/tilt errors are both corrected (PL&TT) in which the iteration rate of tip/tilt controlling is around 1 kHz. The Ave of the cost function reaches 0.994, and the MSE rises slightly to 0.0034 due to the fluctuations of the fiber end face in AFOC during the tip/tilt control. Comparing the cost function curves in the three states, it can be seen that the energy concentration in the pinhole may reach the highest level only when the phase and tip/tilt errors are corrected simultaneously.

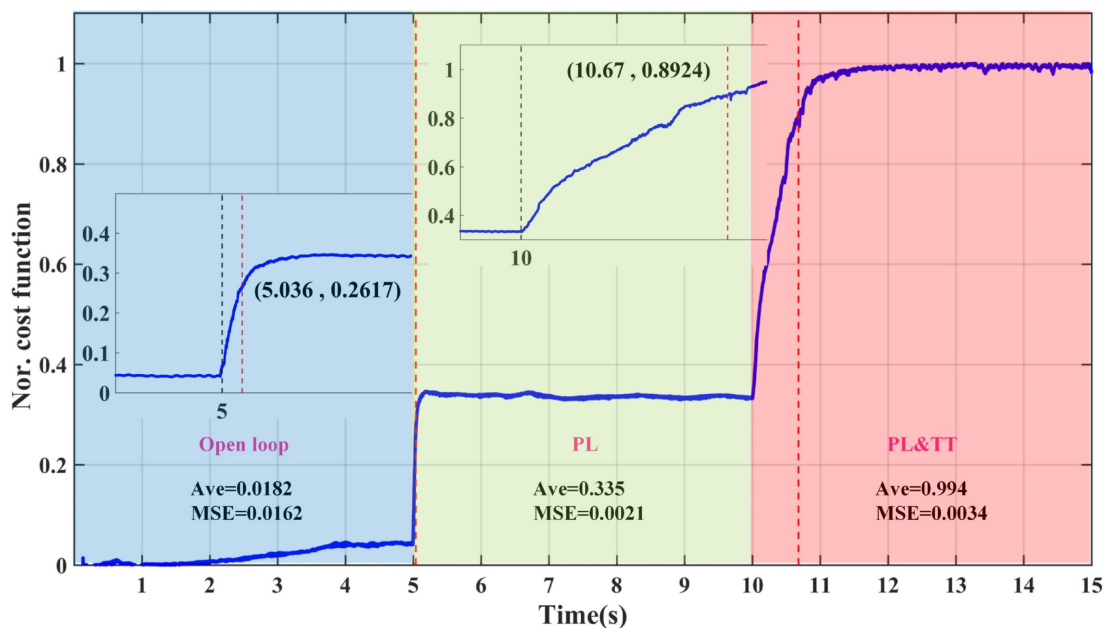


Fig. 9. Normalized cost function acquired by PD.

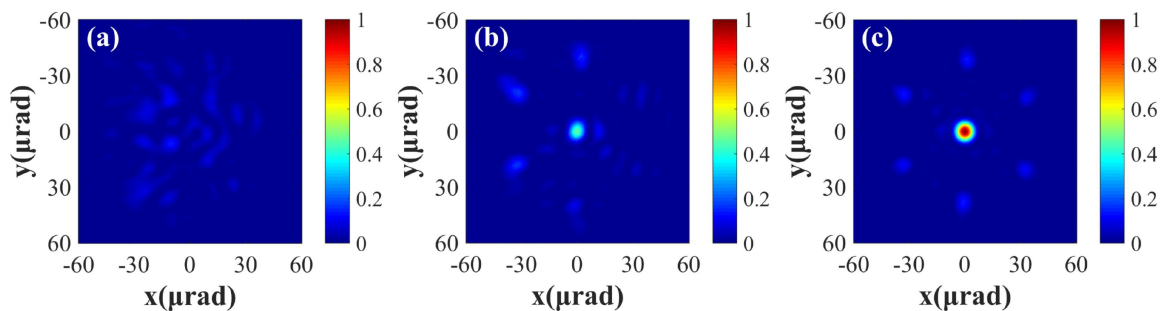


Fig. 10. Normalized long-exposure intensity pattern of the combined beams in the far-field. (a) open loop (b) closed loop (with only phase errors corrected) and (c) closed loop (with both phase errors and tip/tilt errors corrected).

A 5 s long exposure pattern of the combined beam in the far-field is shown in Fig. 10. PIB is obtained by calculating the ratio of the pixel intensity in the bucket to the whole far-field image's pixel intensity, which reflects the relationship between the central lobe power of the combined beam and the total transmitting power. Here, the bucket's size is the pixel area occupied by the Airy Disk when the beam amplitude is evenly distributed. Panel (a) shows the situation when the phase-lock and tip/tilt controls are not performed. It is seen that there is nearly no interference pattern at the camera's target surface, i.e. the system is in an incoherent state, and the energy concentration of the combined beams is very weak. The corresponding mean value of PIB is 0.08. Panel (b) shows the far-field spot long exposure image when the phase-lock control is performed without tip/tilt control. A bright spot appears on the target surface of the camera, which is the central lobe of the combined beam, together with four side lobes around the central lobe, which means that after the phase-locked control, the combined beam is characterized by some coherent combining effects. At this stage, the combined beam has a mean PIB of 0.26, which is 0.18 higher than that of the open loop state. Panel (c) is a far-field long exposure image in which the phase and tip/tilt errors are both

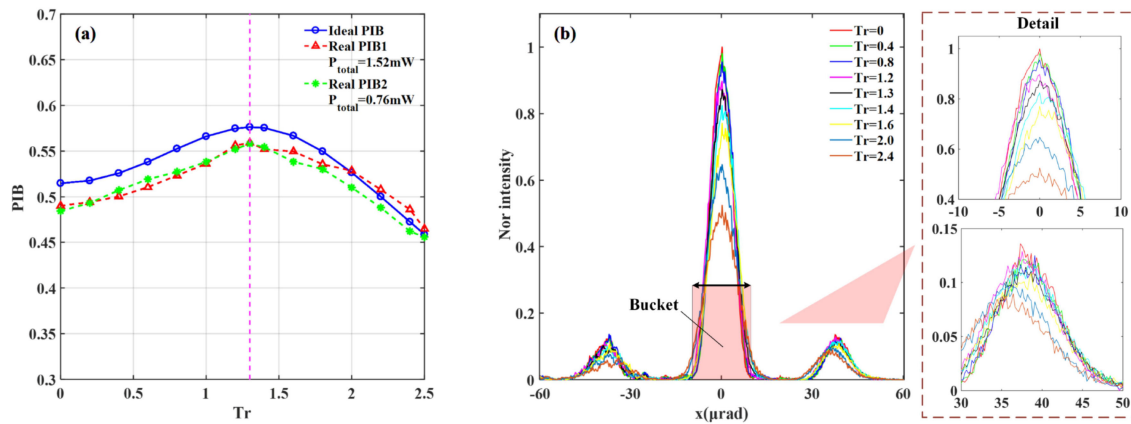


Fig. 11. (a) Comparison of theoretical PIB and experimental PIB. (b) One-dimensional intensity distribution of the combined beams.

corrected (PL&TT). When the closed loop state is stabilized, there are 7 clear spots in the far-field. At this stage, the intensity of the central lobe is significantly higher than that of the other two states, the strength of the side lobe is weakened, and the distribution is more uniform. The average PIB of the combined beam is 0.49, reaching the highest level during the entire experiment.

Using the same transmit power, the amplitude of the transmit array may be redistributed by adjusting AM to obtain a Gaussian distribution of the envelopes with different T_r values. The comparison between the simulation results and the experimental results is shown in Fig. 11 (a) and the normalized long-exposure intensity patterns of the combined beams in far-field are shown in Fig. 12. Experimental results show that as T_r increases, the amplitude envelope of the transmitting array changes from a uniformly distributed flat-topped type to a discretely distributed Gaussian type. PIB also gradually increases from 0.49 ($T_r = 0$) to 0.56 ($T_r = 1.3$), and PIB is increased by 14.3% compared to the maximum value during the entire experiment. Then, as T_r continues to increase, PIB decreases and even go below the initial value 0.49. Moreover, we perform two experiments with different total transmit power values. During each experiment, the total transmit power remains unchanged, and T_r obtained by numerical simulation is used to adjust the amplitude distribution of the beamlets. As shown in Fig. 11(a), when P_{total} is 1.52 mW and 0.76 mW, PIB shows the same trend. This means that the average power density of the combined beam can be improved by amplitude modulation and the best experimental results are obtained only when T_r is appropriate.

Fig. 11(b) shows the normalized one-dimensional beam intensity distribution of the combined beams at different T_r . As T_r increases from 0 to 1.3, the peak power of the side lobes decreases because the power is transferred to the central-lobe. This change is also seen directly in Fig. 12. Experimental results show that central-lobe energy can be further improved via tuning the amplitude envelope of the beamlets in the near-field after the phase and tip/tilt errors are both corrected. This method is suitable for applications where the total input power of the FLPA is limited. For example, when the FLPA is used for space debris cleaning.

4. Summary

The traditional approach to improve PIB of FLPA is increasing the filling factor of the transmitting plane and introducing phase lock and tip/tilt controls into the system. To further enhance PIB of FLPA, we employed a method based on amplitude weighting, which allowed us to increase the central lobe energy. Numerical simulations showed that fiber phased array with Gaussian amplitude envelope shows a considerable enhancement effect on far-field central lobe energy compared to

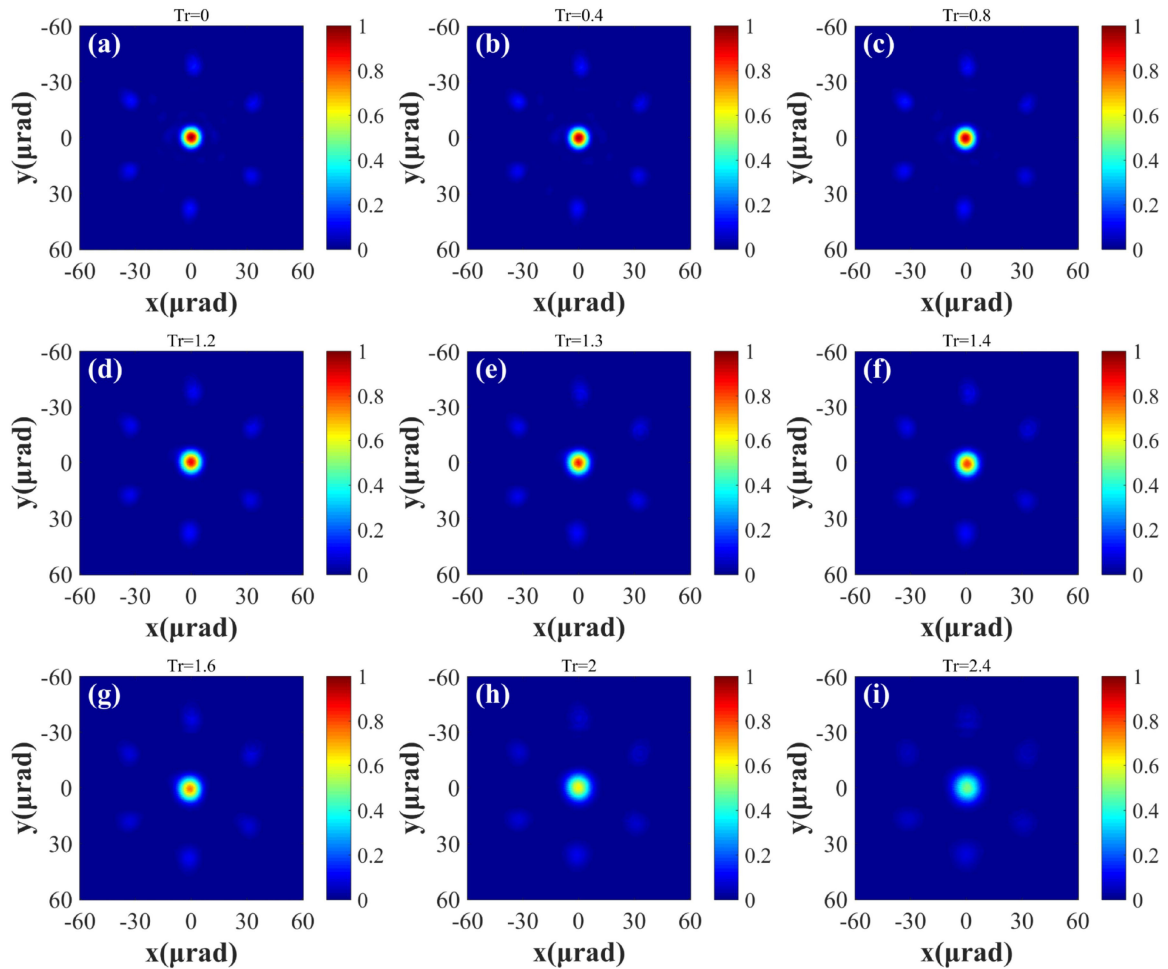


Fig. 12. Normalized long-exposure intensity patterns of the combined beams with different Tr in the far-field.

FLPA systems using uniform amplitude distribution of aperture laser emission. We found the same behavior with 7, 19, 37, and 61 FLPA systems at the same filling factor. Optimal performance was obtained with $Tr = 1.3$. Experimental results showed that PIB gradually increased from 0.49 ($Tr = 0$) to 0.56 ($Tr = 1.3$), after correcting the phase and tip/tilt errors. The experimental results were in agreement with the theoretical analysis and confirmed that amplitude modulation is a promising way to achieve high energy density fiber laser output. Our results demonstrated a new method to optimize PIB of FLPA besides the tip/tilt control and phase-locked controls under limited total power output.

Acknowledgment

The authors declare no conflicts of interest.

References

- [1] Z. Liu, X. Jin, R. Su, P. Ma, and P. Zhou, "Development status of high power fiber lasers and their coherent beam combination," *Sci. China Inf. Sci.*, vol. 62, no. 4, 2019, Art no. 41301.

- [2] H. Chang *et al.*, "First experimental demonstration of coherent beam combining of more than 100 beams," *Photon. Res.*, vol. 8, no. 12, pp. 1943–1948, 2020.
- [3] E. Shekel, Y. Vidne, and B. Urbach, "16 kw single mode cw laser with dynamic beam for material processing," in *Proc. Fiber Lasers XVII: Technol. Syst. Int. Soc. Opt. Photon.*, vol. 11260, 2020, Art no. 1126021.
- [4] G. A. Mourou, D. Hulin, and A. Galvanauskas, "The road to high peak power and high average power lasers: Coherent-amplification-network (can)," in *Proc. AIP Conf. Proc.*, vol. 827, no. 1, 2006, pp. 152–163.
- [5] M. Vorontsov *et al.*, "Comparative efficiency analysis of fiber-array and conventional beam director systems in volume turbulence," *Appl. Opt.*, vol. 55, no. 15, pp. 4170–4185, 2016.
- [6] D. Zhi *et al.*, "Propagation of ring airy Gaussian beams with optical vortices through anisotropic non-Kolmogorov turbulence," *Opt. Commun.*, vol. 387, pp. 157–165, 2017.
- [7] R. Souillard, M. N. Quinn, T. Tajima, and G. Mourou, "Ican: A novel laser architecture for space debris removal," *Acta Astronautica*, vol. 105, no. 1, pp. 192–200, 2014.
- [8] T. Weyrauch *et al.*, "Deep turbulence effects mitigation with coherent combining of 21 laser beams over 7 km," *Opt. Lett.*, vol. 41, no. 4, pp. 840–843, 2016.
- [9] X. Cheng, J.-L. Wang, C.-H. Liu, L. Wang, and X.-D. Lin, "Fiber positioner based on flexible hinges amplification mechanism," *J. Korean Phys. Soc.*, vol. 75, no. 1, pp. 45–53, 2019.
- [10] D. Zhi *et al.*, "Highly efficient coherent conformal projection system based on adaptive fiber optics collimator array," *Sci. Rep.*, vol. 9, no. 1, pp. 1–7, 2019.
- [11] D. Zhang, F. Zhang, and S. Pan, "Grating-lobe-suppressed optical phased array with optimized element distribution," *Opt. Commun.*, vol. 419, pp. 47–52, 2018.
- [12] J. Lei, J. Yang, X. Chen, Z. Zhang, G. Fu, and Y. Hao, "Experimental demonstration of conformal phased array antenna via transformation optics," *Sci. Rep.*, vol. 8, no. 1, 2018, Art no. 3807.
- [13] H. Wang *et al.*, "Beam quality improvement of coherent beam combining by gradient power distribution hexagonal tiled-aperture large laser array," *Opt. Eng.*, vol. 58, no. 6, 2019, Art. no. 0 66105.
- [14] R. J. Mailloux, *Phased Array Antenna Handbook*. Norwood, MA, USA: Artech House, 2017.
- [15] N. Stelmakh, "External-to-cavity lateral-mode harnessing devices for high-brightness broad-area laser diodes: Concept, realizations, and perspectives," *Novel In-Plane Semicond. Lasers VIII, Int. Soc. Opt. Photon.*, vol. 7230, 2009, Art no. 72301B.
- [16] C. L. Dolph, "A current distribution for broadside arrays which optimizes the relationship between beam width and side-lobe level," *Proc. IRE*, vol. 34, no. 6, pp. 335–348, 1946.
- [17] J. Sun *et al.*, "Two-dimensional apodized silicon photonic phased arrays," *Opt. Lett.*, vol. 39, no. 2, pp. 367–370, 2014.
- [18] D. Zhi *et al.*, "Realization of large energy proportion in the central lobe by coherent beam combination based on conformal projection system," *Sci. Rep.*, vol. 7, no. 1, pp. 1–9, 2017.
- [19] J. J. Stamnes, *Waves in Focal Regions: Propagation, Diffraction and Focusing of Light, Sound and Water Waves*. Evanston, IL, USA: Routledge, 2017.
- [20] S. A. Akhmanov and S. Y. Nikitin, *Physical Optics*. Oxford, U.K.: Clarendon Press, 1997.
- [21] J. W. Goodman, *Introduction to Fourier Optics*, Colorado, USA: Roberts Company Publishers, 2005.
- [22] C. Geng, W. Luo, Y. Tan, H. Liu, J. Mu, and X. Li, "Experimental demonstration of using divergence cost-function in spgd algorithm for coherent beam combining with tip/tilt control," *Opt. Exp.*, vol. 21, no. 21, pp. 25045–25055, 2013.
- [23] M. A. Vorontsov and V. Kolosov, "Target-in-the-loop beam control: Basic considerations for analysis and wave-front sensing," *J. Opt. Soc. Amer. A*, vol. 22, no. 1, pp. 126–141, 2005.
- [24] F. Li, C. Geng, G. Huang, Y. Yang, X. Li, and Q. Qiu, "Experimental demonstration of coherent combining with tip/tilt control based on adaptive space-to-fiber laser beam coupling," *IEEE Photon. J.*, vol. 9, no. 2, Apr. 2017, Art. no. 7102812.
- [25] M. A. Vorontsov and V. Sivokon, "Stochastic parallel-gradient-descent technique for high-resolution wave-front phase-distortion correction," *J. Opt. Soc. Amer. A*, vol. 15, no. 10, pp. 2745–2758, 1998.
- [26] C. Geng *et al.*, "Fiber laser transceiving and wavefront aberration mitigation with adaptive distributed aperture array for free-space optical communications," *Opt. Lett.*, vol. 45, no. 7, pp. 1906–1909, 2020.